A study into stress relaxation in oxides formed on zirconium alloys

DOI:
10.1016/j.jnucmat.2014.09.072

Document Version
Final published version

Journal of Nuclear Materials 456 (2015) 415–425

Contents lists available at ScienceDirect

Journal of Nuclear Materials

journal homepage: www.elsevier.com/locate/jnucmat

A study into stress relaxation in oxides formed on zirconium alloys

P. Platt [a,*], E. Polatidis [a], P. Frankel [a], M. Klaus [c], M. Gass [b], R. Howells [b], M. Preuss [a]

[a] University of Manchester, School of Materials, Materials Performance Centre, Manchester M13 9PL, UK
[b] AMEC, Walton House, Faraday Street, Birchwood Park, Risley, Warrington WA3 6GA, UK
[c] Helmholtz Zentrum Berlin für Materialien und Energie, Albert-Einstein Strasse 15, 12489 Berlin, Germany

ARTICLE INFO

Article history:
Received 7 July 2014
Accepted 28 September 2014
Available online 8 October 2014

ABSTRACT

Pressurised and boiling water reactors contain zirconium alloys, which are used as nuclear fuel cladding. Oxidation of these alloys, and the associated hydrogen pick-up, is a limiting factor in the lifetime of the fuel. To extend the burn-up of nuclear fuel requires control of the oxidation, and therefore development of a mechanistic understanding of the cladding corrosion process. Synchrotron X-ray diffraction (S-XRD) has been used to analyse oxide layers formed during in-situ air oxidation of Zircaloy-4 and ZIRLO™. Analysis shows that as the oxide thickness increases over time there is a relaxation of the stresses present in both the monoclinic and meta-stable tetragonal phases, and a reduction in the tetragonal phase fraction. To better understand the mechanisms behind stress relaxation in the oxide layer, finite element analysis has been used to simulate mechanical aspects of the oxidation process. This simulation was first developed based on stress relaxation in oxides formed in autoclave, and analysed ex-situ using S-XRD. Relaxation mechanisms include creep and hydrogen-induced lattice strain in the metal substrate and creep in the oxide layer. Subsequently the finite element analysis has been extended to stress relaxation observed by in-situ S-XRD oxidation experiments. Finite element analysis indicates that the impact of creep in the oxide is negligible, and the impact of both creep and hydrogen-induced lattice strain in the metal substrate metal is small. The implication is that stress relaxation must result from another source such as the development of roughness at the metal–oxide interface, or fracture in the oxide layer.

1. Introduction

Zirconium alloys are used as fuel cladding in pressurised and boiling water nuclear reactors. As such these materials are exposed to a large number of environmental factors that will promote degradation mechanisms such as oxidation. At high burn-ups, i.e. extended service life, oxidation and the associated hydrogen pick-up can be a limiting factor in terms of fuel efficiency and safety. The oxidation kinetics for many zirconium alloys are cyclical, demonstrating a series of approximately cubic kinetic curves separated by transitions [1–5]. These transitions are typified by a breakdown in the protective character of the oxide and are potentially linked to a number of mechanical issues. Understanding how these issues influence oxidation is a key to developing a full mechanistic understanding of the corrosion process.

Synchrotron X-ray diffraction (S-XRD) experiments have shown that oxides formed on zirconium alloys are strongly compressed and composed of both monoclinic and stabilised tetragonal phases. Published results suggest residual stresses ranging from −3800 MPa to −80 MPa, and tetragonal phase fractions ranging from 50% to 5%, depending upon the position on the corrosion kinetics curve and alloy composition [4–8]. Although there is some variation close to transition in the corrosion kinetics, each of these papers show that over several microns of oxide growth there is a gradual reduction in both the average compressive stress and the tetragonal phase fraction. It is implied from this that some combination of mechanisms are relaxing the compressive stress and destabilising the tetragonal phase. Possible mechanical factors include oxidation-induced creep and strain, or crack formation in the oxide layer [9–11]. The tetragonal to monoclinic phase transformation is considered as a key component in the oxidation process as it could potentially cause the crack and pore formation observed using TEM [11,12]. This would provide fast ingress routes for oxygen containing species thereby accelerating the corrosion kinetics, and degradation of zirconium alloy components.

A number of attempts have been made to experimentally define oxidation-induced strain in the metal substrate as a result of creep and hydrogen pick-up. Donaldson et al. oxidised samples of cold work stress relieved Zircaloy-4 tube in air, with wall thicknesses between 0.58 and 0.08 mm, at temperatures in the range of

* Corresponding author at: Material Performance Centre, Room D10, Manchester Materials Science Centre, The University of Manchester, Grosvenor Street, Manchester M1 7HS, UK. Tel.: +44 7753431684.
E-mail address: Philip.Platt@manchester.ac.uk (P. Platt).

http://dx.doi.org/10.1016/j.jnucmat.2014.09.072
0022-3115/

350–450 °C for times ranging from 152 to 753 days. Axial strains were measured at regular intervals. Across the temperatures measured, total strains at the end of the tests ranged between 0.0016–0.0265 in the thinnest tube and 0.0003–0.0047 in the thickest. In particular, the elevated strain with decreasing substrate thickness is evidence of oxidation-induced creep as reducing substrate thickness would increase the oxidation-induced stress in the metal substrate [13]. Both Blat et al. and Barberis et al. have attempted to measure strains resulting from both oxidation-induced creep of the metal substrate and hydrogen-induced lattice strain [9,10]. Blat et al. oxidised recrystallised 0.45 mm thick Zircaloy-4 sheet at 360 °C, with simulated primary water chemistry. Oxide thicknesses ranged from 2.1 to 7.3 μm, i.e. 100–400 days exposure. Including both hydrogen pick-up and oxidation-induced creep, strains ranged from 0.00012 to 0.00066. Barberis et al. carried out a significant number of tests into oxidation-induced strain due to creep and hydrogen pick-up. Oxidising recrystallised M5 tube in 360 °C water for ~220 days resulted in an oxide ~3.7 μm thick and a diametral strain of ~0.00015 [10]. Although measuring such small levels of strain is problematic, these papers show clear evidence of creep deformation in the metal substrate as a direct result of oxidation.

In-reactor zirconium alloys are exposed to a range of stresses from sources such as channel bowing, oxidation, and pellet clad interaction (PCI). These factors can limit the lifetime and safety of the fuel, hence research into creep mechanisms in zirconium alloys is significant [14–16]. The most commonly researched creep mechanism is power law creep, which is based on dislocation climb and glide. Although near surface S-XRD of the metal substrate has given stress values of 50–100 MPa [5], this does not correlate with calculations for the bulk metal balancing stress based on the average in-plane stress in the oxide layer measured using S-XRD. Instead, Barberis et al. calculate bulk tensile stresses present in the metal substrate that are of the order of ~15 MPa [10]. Extrapolating the stress measured at the near surface to the bulk of the metal substrate is problematic due to potential for localised stress effects relating to roughness at the metal–oxide interface [17]. Taking the bulk stress to be ~15 MPa puts oxidation-induced creep in a low stress regime. Numerous mechanisms have been presented in the literature to explain creep in this regime including Coble, Nabarro-Herring, Harper-Dorn, Ashby-Verrall and Grain Boundary Sliding (GBS) [16]. Assignment of a specific creep mechanism is based on stress, temperature, and grain size [15,16,18–22]. In the three main pieces of work that study oxidation-induced creep, all strains in the substrate are measured empirically; and no discussion is given to assigning an actual creep mechanism to the observed behaviour [9,10,13].

For many years manufactured samples of tetragonal and cubic zirconia (ZrO_2) have been known to be superplastic and capable of significant levels of strain under the appropriate experimental conditions. Strain rates of up to $1 \times 10^{-3}\ s^{-1}$ have been recorded at 1150 °C for nanocrystalline, yttria stabilised tetragonal zirconia [23]. This has led to a significant amount of research into creep [23–28], and a number of tracer element diffusion tests designed to define the diffusion coefficients have been conducted [29–32]. However this temperature is much higher than would be observed in reactor under normal operating conditions, and the morphology of the oxides are very different. As yet there appears to be no experimental work that directly confirms the presence of creep in the oxide layer during oxidation at 360 °C.

The hydrolytic component of the zirconium corrosion process leads to the generation of hydrogen, a percentage of which is known to be absorbed into the metal substrate [1]. As an interstitial element it occupies the tetrahedral sites between lattice planes and causes growth of the metal substrate. Blat et al. used a gaseous hydrogen charging technique to measure the hydrogen-induced lattice strain. Results taken between 300 and 2000 wppm hydrogen predict strains in recrystallised Zircaloy-4 sheet of 1.15×10^{-6} per wppm [9]. Vizceno et al. aimed to quantify this effect by heating cathodically charged Zircaloy-4 tube to 300 °C in a push-rod differential dilatometer. Hydrogen concentrations in the range of 150–400 wppm gave an axial elongation of 5.21×10^{-6} per wppm [33].

The following work combines newly presented in-situ S-XRD data on the development of phase fraction and stress as an oxide grows, existing ex-situ S-XRD measurements on autoclave tested samples, and significant finite element analysis of the oxidation process. The aim of the work is to establish if a combination of mechanisms including creep and hydrogen-induced lattice strain could explain oxide stress relaxation observed experimentally.

2. Experimental

2.1. Materials

Materials included samples of recrystallised Zircaloy-4 and ZIRLO™ sheet, cut into coupons with respective dimensions of $30 \times 20 \times 0.6\ mm^3$ and $30 \times 20 \times 0.45\ mm^3$. Sample preparation involved pickling in HF solution (5%HF, 45%HNO_3 and 50%H_2O) [34]. All materials were provided by Westinghouse, and the chemical compositions for these materials can be found in Table 1.

2.2. In-situ synchrotron X-ray diffraction

All synchrotron X-ray diffraction experiments were carried out at the EDDI beam-line at BESSY II (Berlin, Germany) [35]. EDDI is a polychromatic energy dispersive beam-line allowing rapid acquisition of the diffraction peaks in the energy range of 8–120 keV. The classical $\sin^2\psi$ technique was used to characterise the biaxial in-plane compressive residual stress in the oxide layer by tilting the sample through a range of ψ angles and measuring diffraction patterns through each angle. The specific peaks of interest for measuring residual stress in thermally grown zirconium oxides are the $(\bar{1}\,1\,1)_m$ monoclinic and $(1\,0\,1)_t$ tetragonal peaks. In addition to these two reflections the $(1\,1\,1)_m$ monoclinic peak was incorporated into the Garvie–Nicholson formula for defining the tetragonal zirconia phase fraction [36]:

$$f_{tet} = \frac{I_{t(1\,0\,1)}}{I_{t(1\,0\,1)} + I_{m(1\,1\,1)} + I_{m(\bar{1}\,1\,1)}} \quad (1)$$

where I_{xxx} are the averaged integrated intensities of each reflection along the range of ψ angles. These techniques have been used for both the previously published ex-situ analysis of samples oxidised in an autoclave [5], and the in-situ air oxidation experiments presented here. More detailed description of the $\sin^2\psi$ and Garvie–Nicholson techniques used in similar experiments can be found in [5]. The key in-situ oxidation experiments used a heated sample stage, allowing diffraction patterns to be recorded every 4.5 min as the oxide layer is formed. Samples from each of the alloys were subjected to the thermal profiles discussed in the following section, and the evolution of each oxide phase was recorded. By calculating the stress in the monoclinic and tetragonal phases and weighting them based on the corresponding phase fraction it is possible to define an average bulk oxide in-plane compressive stress.

The previously presented S-XRD experiments involved removing a number of samples from the autoclave at different oxidation

Table 1
Chemical compositions for zirconium alloys (wt%).

Materials	Sn	Fe	Cr	Ni	Nb
Zircaloy-4	1.24	0.17	0.1		<0.01
ZIRLO™	0.92	0.09			0.91

times and analysing them ex-situ. The results indicated a gradual relaxation in the in-plane biaxial compressive stress with increasing oxidation time and oxide thickness [5]. This has formed the basis for the development of a finite element analysis. The in-situ tests reported in this publication show more detailed information on stress relaxation over time for single samples, thereby removing the issues of variation between samples. A similar finite element analysis has then been extended to simulate these in-situ experiments.

2.3. Oxidation

Fig. 1a shows the oxidation kinetics for Zircaloy-4 oxidised in an autoclave at 360 °C in simulated primary water [5,34]. S-XRD measurements reported by [5] are used here to inform simulations by finite element analysis. Available samples were sent to Westinghouse for analysis of hydrogen concentration using a hot vacuum extraction procedure. Fig. 1b shows the resulting concentrations, along with calculated values described in Section 3.3. Fig. 2 shows a schematic of the sample setup for the in-situ S-XRD experiment, illustrating the two positions at which two temperature readings were taken during heating. In-situ S-XRD oxidation was carried out in air. Here T1 and T2 represent the temperature of the heating plate and of the sample surface, respectively. For each of the applied thermal profiles there was a significant difference between the reading for the sample stage and the thermocouple. Therefore, in order to determine the weight gain with time during oxidation for each in-situ S-XRD experiment, a number of air oxidation tests were carried out using a Vecstar Ltd. air furnace for both alloys. T1 and T2 recorded during the S-XRD experiment were used to determine the upper and lower temperature limits. Samples were removed from the furnace every 7.5 min. Eddy current measurements (ECT probe) of the original in-situ samples were carried out to determine the final oxide thickness after testing, which is very similar to the method used previously by Park et al. [37]. Using T1 and T2 as upper and lower temperature limits, a sensitivity study was carried out to determine the temperature profile vs. oxidation time required to give the appropriate level of oxidation. Fig. 3 shows the temperature profiles taken from the heating stage, the thermocouple at the sample surface and the estimated temperature profile based on the oxide thicknesses. Based on the oxide thicknesses the samples appear to have been exposed to thermal

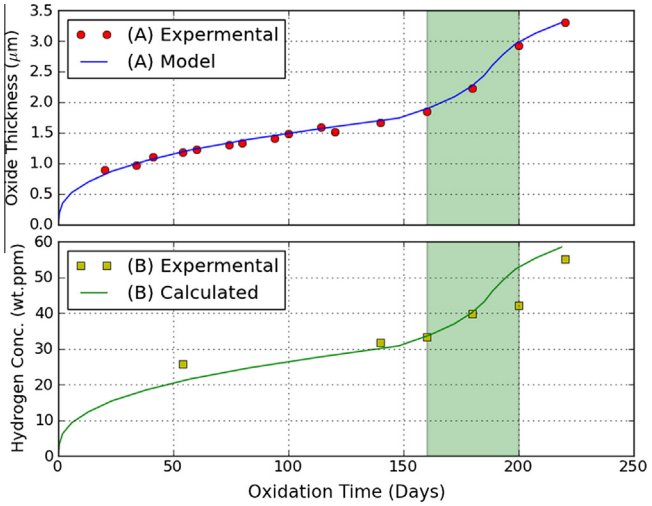

Fig. 1. Oxidation kinetics (a) and hydrogen concentrations (b) for samples of Zircaloy-4 tested in 360 °C simulated primary water, with the shaded green area identifying transition in the corrosion kinetics [5]. In addition to the experimental data, the model oxidation kinetics and calculated hydrogen concentrations are also included.

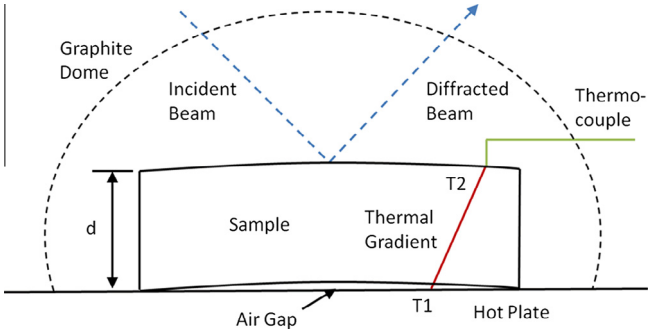

Fig. 2. Illustration of the in-situ S-XRD experimental setup.

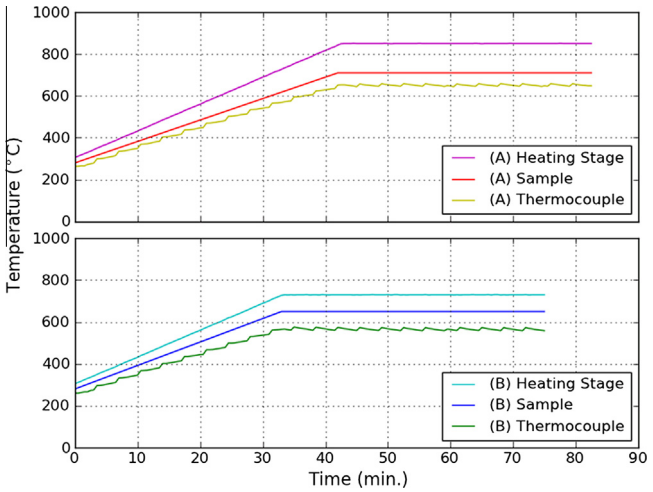

Fig. 3. Thermal profiles over time from the heating stage and thermocouple, and the estimated thermal profile based on oxidation tests for Test A (top) and Test B (bottom).

profiles up to 710 °C (A) and 650 °C (B), with a heating rate of ~11.2 °C/min and a hold time at temperature of ~40 min. Figs. 4 and 5 show the different results for the furnace oxidation of Zircaloy-4 and ZIRLO™ samples, with oxide thickness being based on weight gain measurements.

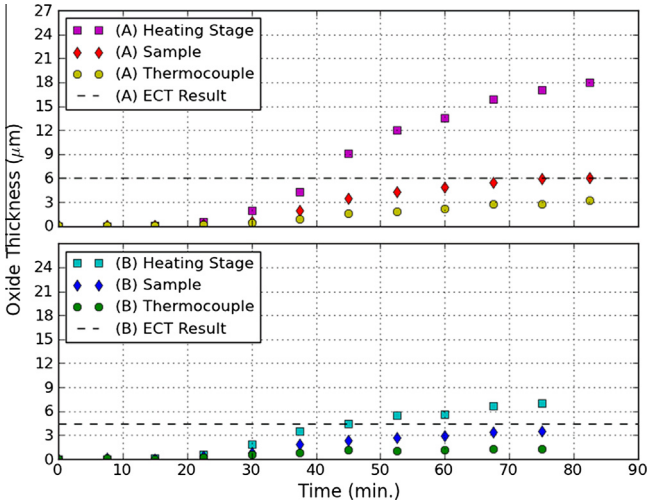

Fig. 4. Zircaloy-4 air furnace oxidation results based on the different thermal profiles over time, for Test A (top) and Test B (bottom).

3. Model construction

3.1. Sample representation & boundary conditions

To simulate the mechanical aspects of the oxidation process the Abaqus finite element code was used to create an elastic generalised plane strain model representing a thin slice in the middle of a sheet sample; see Fig. 6 for a schematic illustration. This model represents a section of the sample with a width of 2 μm, a height of 0.33 mm (Zircaloy-4) or 0.227 mm (ZIRLO™), and is composed of 4 node bilinear elements. The coordinate system has direction *X* parallel to the metal–oxide interface and direction *Y* perpendicular to the metal–oxide interface. A symmetry boundary condition was applied to the bottom surface of the model, fixing movement in direction *Y*, to represent a sample oxidised on both sides. A second symmetry boundary condition was applied to the left edge, fixing movement in direction *X*, and a linear constraint equation was applied to the right edge to ensure the entire face strained evenly in direction *X*. This combination of boundary conditions and constraints allows the model to represent a small section in a relatively large sample.

The near surface region has been partitioned into 20 layers of equal thickness based on the maximum oxide thickness of each of the samples being modelled. These layers simulate a perfectly flat metal–oxide interface. Although the actual metal–oxide interface has been seen to be rough, with an amplitude in the order of 0.1 μm [38], it is not the intention of this work to analyse the impact of these features. Each of the partitioned layers has two steps associated with it.

Step 1 is a static linear elastic step in which a metal layer transforms into an oxide that includes a change in the material properties and a volumetric expansion based on the Pilling-Bedworth ratio. The expansion is defined using an orthotropic strain tensor first published by Parise et al. [17]. It gives an out-of-plane expansion of 0.54 perpendicular to the metal–oxide interface, and a lateral in-plane expansion of 0.005. It is the lateral expansion, and consequent constraint provided by the metal substrate, that will generate the strong compressive stress in the oxide and the weak tensile stress in the relatively thick metal substrate. As such this value of 0.005 represents the level of strain required to completely relax the stress in the first oxide that forms.

Step 2 is a time dependent visco-plastic step, and uses a time interval based on the thickness of the partition and the predicted oxidation kinetics shown in Figs. 1, 4 and 5. It is during this visco-plastic step that any creep based relaxation may occur. All calculations and models presented are in mm and MPa, with time in hours. Table 2 shows the bulk elastic properties used. This combination of partitioned layers and steps allows the model to represent the mechanical aspect of an advancing oxide-metal interface.

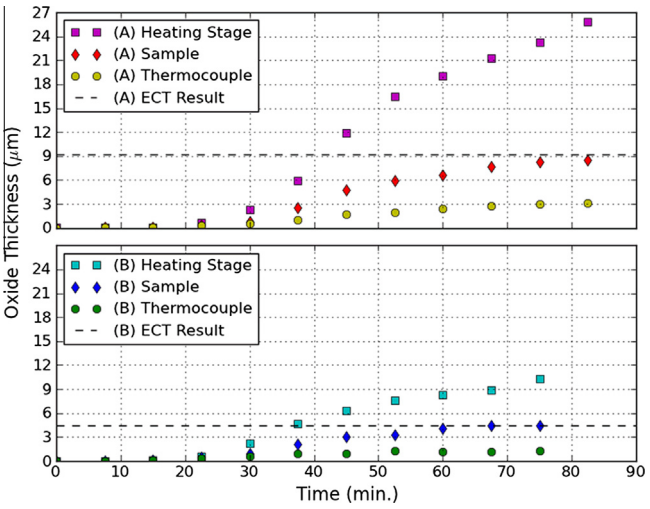

Fig. 5. ZIRLO™ air furnace oxidation results based on the different thermal profiles over time, for Test A (top) and Test B (bottom).

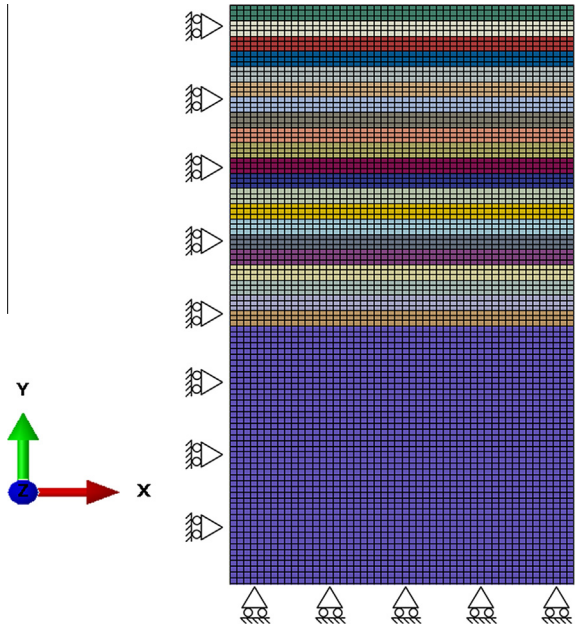

Fig. 6. Illustration of the Abaqus model used. Each thin coloured layer represents a partitioned region and oxidation increment. The thicker section at the bottom represents the substrate which extends much further than shown.

It should be noted that this type of simulation does not take into account localised effects that could potentially increase or decrease the stress in the oxide. The metal–oxide interface is known to form undulations or roughness [38], and absorb oxygen into the near surface metal [39], both of which could potentially relax stress in the oxide be deformation and increase of the interfacial area. Research presented in this paper indicates that at least some of the tetragonal phase present in the oxide transforms into monoclinic. This phase transformation has an associated volume expansion that could introduce additional stress into the oxide [11,40]. These localised effects are not the focus of this work and as such have not been incorporated into the simulations.

3.2. Elastic analytical validation

Without the application of creep or hydrogen-induced lattice strain the above models are fully elastic, and for an oxide 0.001 mm thick will give an in-plane compressive stress of -1749 MPa in the oxide layer and an in-plane tensile stress of 5.3 MPa in the metal substrate. This model can be validated mathematically. Let $E' = \frac{E}{1-\nu}$ to account for the stress being in two dimensions. The compatibility relationship can be defined by Eq. (2). The in-plane strain in the oxide must equal the in-plane strain the metal substrate.

Table 2
Elastic properties [5].

Material property	Bulk zirconium	Bulk oxide
Elastic modulus (MPa)	960,00	253,000
Poisson's ratio	0.34	0.282

$$\frac{\sigma_2}{E_2'} = \Delta - \frac{\sigma_1}{E_1'} \tag{2}$$

where Δ is the strain due to the oxidation expansion, σ_1 is the in-plane stress in the oxide (compressive), σ_2 is the in-plane stress in the substrate (tensile), E_1 is the Young's modulus of the oxide, and E_2 is the Young's modulus of the substrate. The equilibrium relationship can be defined by Eq. (3). The in-plane force in the oxide must be equal to the in-plane force in the metal substrate.

$$2\sigma_1 t_1 = t_2\sigma_2 \tag{3}$$

where t_1 is the oxide thickness and t_2 is the substrate thickness, assuming oxidation occurs on both sides of the sample. Combining Eqs. (2) and (3) can give the in-plane stress in the oxide.

$$\left(\frac{2t_1}{E_2' t_2} + \frac{1}{E_1'}\right)^{-1} \times \Delta = \sigma_1 \tag{4}$$

Or combining Eqs. (2) and (3) can give the in-plane stress in the metal substrate

$$\left(\frac{1}{E_2'} + \frac{t_2}{2E_1' t_1}\right)^{-1} \times \Delta = \sigma_2 \tag{5}$$

where E_1 = 253,000 MPa (oxide Young's modulus), E_2 = 96,000 MPa (metal Young's modulus), υ_1 = 0.282 (oxide Poisson's ratio), υ_2 = 0.34 (metal Poisson's ratio) [5], t_1 = 0.001 mm (oxide thickness), t_2 = 0.66 mm (metal thickness), Δ = 0.005 (lateral expansion), resulting in an oxide stress, σ_1 = −1740 MPa. The elastic properties used in all simulations are bulk values. Both the oxide layer and metal substrate are known to be highly textured, potentially leading to a range of different elastic properties. A short sensitivity study using Eq. (2) indicated that increasing the Elastic modulus and/or the Poisson's ratio would increase the magnitude of the in-plane stresses in both the metal and the oxide. Using the same approach as Parise et al. [17], this would simply require a reduction in the in-plane expansion component in order to match the in-plane compressive stress in the oxide with the values determined experimentally. After modification of the in-plane expansion component the impact on the stress balance, i.e. the ratio of stresses in the oxide and the metal, is negligible and therefore these changes would not impact the simulated stress relaxation.

3.3. Hydrogen pick-up

Corrosion of zirconium alloys in water, at 360 °C, proceeds via the following reaction [1]:

$$Zr + 2H_2O \rightarrow ZrO_2 + 2H_2 \tag{6}$$

Assuming the pick-up fraction of released hydrogen being absorbed into the metal substrate is around ~0.2 [41], and for simplicity a constant pick-up fraction throughout the process the total amount of hydrogen picked up at any point along the corrosion curve can be estimated using the following equation:

$$n_H = \left(\frac{2fL_O C}{0.5L_M}\right) \tag{7}$$

where n_H is the hydrogen concentration in moles H/mm^3, f is the hydrogen pick-up fraction (0.2), L_O is the oxide thickness (in mm), L_M is the metal substrate thickness, and C is the concentration of oxygen in zirconium dioxide (9.5×10^{-5} moles O/mm^3). Fig. 1b shows how the calculated hydrogen concentrations (wt ppm) compare with the values described in Section 2.3. The only significant deviation is at 200 days oxidation time. It has been previously observed that different areas of a sample surface go through transition at different points in time [5,34]. Given that only 10–15% of the sample is analysed for hydrogen concentration, the deviation can be explained by natural variation in the oxide thickness across the sample surface. For an oxide 3.3 μm thick on a metal substrate 0.66 mm thick this gives a hydrogen concentration of ~58 wppm. This is in fairly good agreement with the values shown by Videm et al. [42]. A simple way to relate hydrogen concentration (moles H per mm^3) to volumetric expansion is to use the partial molar volume of H in α-Zr ($\overline{V}_H$=1670 mm^3/mol [43]). By making the simplified assumptions that the expansion due to hydrogen pick-up is averaged throughout the sample, and that the volumetric expansion is isotropic, the below equation can be used to estimate the shape change in the X, Y or Z directions.

$$\varepsilon_{ijk} = \left(\sqrt[3]{1 + n_H \overline{V}_H}\right) - 1 \tag{8}$$

For hydrogen concentrations in the range of 150–400 wppm Vizceno et al. gave an axial strain of 5.21×10^{-6} per wppm [33]. For hydrogen concentrations in the range of 300–2000 wppm Blat et al. gave strains of 1.15×10^{-6} per wppm [9]. For a theoretical test concentration of 300 wppm; using the partial molar volume gives a strain in each direction of 0.00108, the Vizceno data gives 0.00156 strain, and the Blat data gives 0.00035 strain. Although the variation between the three values is reasonably large, it gives some support towards basing the expansion in the metal substrate on the partial molar volume of hydrogen in zirconium. This is incorporated into the simulation by applying a strain tensor to the metal substrate. The good correlation with literature, and the impact of the hydrogen induce lattice strain on oxide stress shown later in the paper, indicates that the use of isotopic hydrogen induced expansion is appropriate for this work. The value of the strain is based on the hydrogen concentration for that stage of oxidation. The interpretation therefore is that this will relax the stress in any existing oxide and effectively reduce the in-plane expansion of future oxide growth.

3.4. Creep incorporation

3.4.1. Metal creep

In this analysis creep has been incorporated into both the oxide layer and the metal substrate. It is possible to determine the most likely mechanisms present by consideration of the stress level, grain size, temperature and material. Calculations indicate a stress level in the order of ~6 MPa putting the mechanism below the transition to power law creep [16]. The temperatures used during these experiments range from 360 to 710 °C, and previous characterisation of the Zircaloy-4 material discussed in Section 2 gave a mean grain size in the order of ~15 μm. This would appear to discount Harper-Dorn and Nabarro-Herring based mechanisms [16,19]. Although some form of Ashby-Verall or grain boundary sliding mechanism may be plausible, Coble creep is the best established mechanism and has been incorporated into the metal substrate based on Eq. (9).

$$\dot{\varepsilon}_{co} = \frac{\alpha_{co}\delta D_{gb}}{kT}\frac{\Omega\pi}{g^3}\sigma \tag{9}$$

where T is the temperature, k is the Boltzmann constant, g is the average grain size, Ω is the atomic volume of Zr, σ is the stress, α_{co} is a coefficient, δ is the grain boundary width, and D_{gb} is the grain boundary diffusion coefficient. The grain boundary diffusion coefficient is based on the experimentally derived value for the activation for grain boundary diffusion Q, as shown in Eq. (10), which has an Arrhenius type relationship. In this equation D_o is a pre-exponential coefficient and R is the gas constant.

$$\delta D_{gb} = D_o \exp\frac{-Q(\mathrm{J\ mol^{-1}})}{RT} \tag{10}$$

Defining the activation energy for grain boundary diffusion (Q_{gb}) is complex, and as shown in Table 3, values presented in literature demonstrate a significant range. Two sets of values have been used in these simulations. FEA-1 is defined in order to fit the experimentally observed ex-situ S-XRD data for Zircaloy-4 oxidised in primary water at 360 °C. It includes a modified Coble creep coefficient of $\alpha_{co} = 6$, a grain boundary diffusion activation energy presented by Fiala et al. of $Q_{gb} \approx 124$ kJ/mol, and a pre-exponential coefficient of $D_o = 8.2 \times 10^{-5}$ mm^3 s^{-1} [19]. FEA- 2 is defined in order to give oxidation-induced strain rates in the range of 1.6×10^{-8}–$7\text{x}10^{-8}$ h^{-1} as defined previously in literature for zirconium alloys oxidised at ~360 °C [9,10,13]. This includes the Coble creep coefficient of $\alpha_{co} = 14$ as described by Franklin et al. [15], a grain boundary diffusion activation energy defined by Ravi and presented by Charit et al. of $Q_{gb} \approx 144$ kJ/mol [44], and a pre-exponential coefficient of $D_o = 1.0 \times 10^{-4}$ mm^3 s^{-1}.

3.4.2. Oxide creep

As discussed earlier, manufactured Zirconia is known to be superplastic under appropriate experimental conditions. Although temperatures in the range of 360–710 °C would be very low for creep to occur in the oxide, typical grain sizes are very small on the order of ~30 nm, and stresses are very high in the range of 1–2 GPa. Although research into creep in manufactured zirconia is significant, there is variation between studies in key factors such as the phase fraction, stabilising elements, grain size, temperature, stress, and calculated activation energy. These tend to range from 0–8 wt% yttria or calcium, 75 nm-15 μm grain size, 950–1600 °C test temperature, with the creep test stresses reaching 200 MPa. Typically, the grain size power ranges between 2 and 3, and the stress exponents range from 1 to 2, leading most authors to the conclusion that either Coble or Grain Boundary Sliding creep mechanisms are in operation [23–28]. Identification of transitions in the creep mechanisms are very rare and difficult to validate [24]. A fundamental issue with all of the creep tests, particularly with very small grain sizes, is the tendency for dynamic grain growth to occur. This has been known to generate additional strain in the materials and although attempts are frequently made to correct for this, it adds significant uncertainty to the analysis [23–28]. Another issue is the presence of the doping elements which are known to segregate to grain boundaries and have been linked with reduction in diffusion due to a solute dragging mechanism [26].

For the purposes of this work a Coble creep mechanism has again been incorporated making use of Eqs. (9) and (10). The only available data for zirconia is in the form of manufactured ceramics. The value selected for the activation energy of grain boundary diffusion are defined for 3% yttria stabilised tetragonal zirconia with $Q_{gb} = 506$ kJ/mol and a pre-exponential coefficient of $D_o = 2.9 \times 10^4$ mm^3 s^{-1}.

3.4.3. Finite element application of creep

Creep was modelled in Abaqus using the time hardening equation shown below

$$\dot{\varepsilon}^{cr} = A_{abq}\sigma^n t^m \tag{11}$$

Table 3
Summary of grain boundary diffusion activation energy for zirconium alloys.

Q_{gb} (kJ/mol)	Author
103	Prasad et al. [52]
117	Bernstein et al. [52]
124	Fiala et al. [19]
126	Charit et al. [44]
144	Ravi et al. [44]

where $\dot{\varepsilon}^{cr}$ is the creep strain rate, t is the time, and A_{abq} is a constant. As discussed, Coble creep has been identified as a likely creep mechanism to be dominant during the experimental work discussed in Section 2. As Coble creep is a diffusion based mechanism there should be no hardening, hence $n = 1$ (stress exponent) and $m = -0.0001$ (hardening factor), effectively making $t^m \approx 1$. Combining Eqs. (9) and (11) effectively gives the following term that can be implemented into the finite element analysis.

$$A_{abq} = \frac{\alpha_{co}\delta D_{gb}}{kT}\frac{\Omega\pi}{g^3} \tag{12}$$

4. Results and discussion

4.1. Synchrotron X-ray diffraction

Fig. 7 shows the tetragonal phase fraction and stress state in the oxide of Zircaloy-4 after oxidation in primary water at 360 °C taken from [5]. The original work presents the in-plane biaxial compressive stress experienced by the tetragonal and monoclinic phases separately. Putting this data into Eq. (13) allows definition of an average oxide stress.

$$\sigma_{avg} = (f_t\sigma_t) + (f_m\sigma_m) \tag{13}$$

where σ_{avg} is the average oxide stress, σ_t is the stress in the tetragonal phase, σ_m is the stress in the monoclinic phase, f_t is the tetragonal phase fraction and f_m is the monoclinic phase fraction. From Fig. 7 it can be seen that there is a gradual reduction in both the tetragonal phase fraction and the average residual stress present in the oxide.

Fig. 8 displays typical diffraction patterns for a sample of Zircaloy-4 oxidised in-situ up-to 710 °C, at an incident angle of 3° and ψ angles between 26.5° and 63.4°. The patterns show two monoclinic peaks, one detectable tetragonal peak, and two relatively strong zirconium peaks. Comparisons of the patterns show considerable variation in signal intensity depending upon the ψ angle, which is attributed to the strong crystallographic texture in the oxide

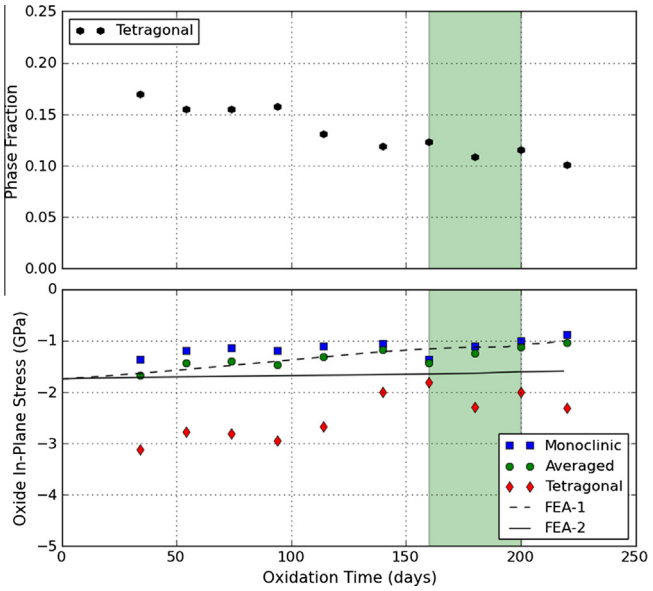

Fig. 7. Zircaloy-4 oxidised at 360 °C in-autoclave, showing tetragonal phase fraction (top) and monoclinic, tetragonal, and averaged in-plane oxide biaxial compressive stresses as well as predicted stresses (bottom), with the shaded green area identifying transition in the corrosion kinetics [5]. FEA-1 uses model parameters fit to the S-XRD data, FEA-2 gives strain rates similar to those presented by Barberis et al. [10], and Donaldson et al. [13].

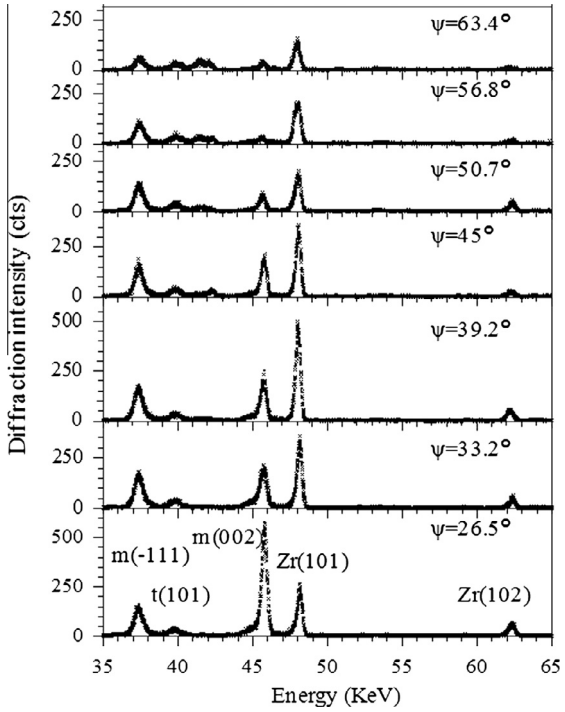

Fig. 8. Example diffraction patterns for a sample of Zirclaoy-4 oxidised in-situ up-to 710 °C (Test A).

and metal substrate. Fig. 9 shows the integrated intensities for the monoclinic $(\bar{1}\,1\,1)_m$ peak and tetragonal $(1\,0\,1)_t$ peaks for the Zircaloy-4 and ZIRLO™ samples oxidised under thermal profiles A and B. The elevated integrated intensities observed for oxides formed on ZIRLO™ compared with Zircaloy-4 at 710 °C supports the idea that ZIRLO™ should exhibit a thicker oxide layer at this temperature. The initial oxide formed during the oxidation experiment did not provide enough diffraction signal and it was only after about 15 min that fittable peak were observed, although the initial peak fits resulted in relatively high uncertainties. It should be noted that the calculation of an average oxide stress, as required for the simulations, is dependent on obtaining monoclinic and tetragonal stresses and the correlating phase fraction. As such each average oxide data point requires the inclusion of the $(\bar{1}\,1\,1)_m$, $(1\,1\,1)_m$ and $(1\,0\,1)_t$ peaks, with a high intensity and a good fit to maximise accuracy, with the result that only data after ~42 min have been included.

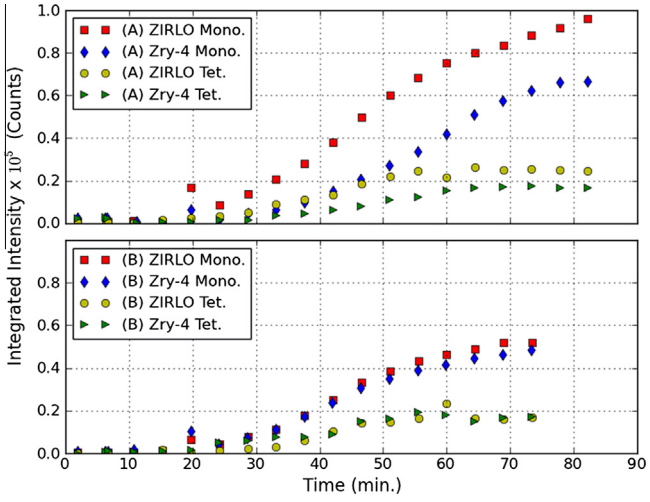

Fig. 9. Integrated intensity of monoclinic and tetragonal peaks recorded for oxides formed on Zircaloy-4 and ZIRLO™ up to 710 °C (Test A, top) and 650 °C (Test B, bottom).

Figs. 10–13 show the tetragonal phase fraction and the monoclinic, tetragonal and average oxide stresses for Zircaloy-4 and ZIRLO™ at temperatures up-to 710 °C (Test A) and 650 °C (Test B). Typically, the range of stresses and phase fractions are similar across samples and test conditions. The general trend is towards a gradual reduction in the tetragonal phase fraction, and stress levels demonstrated by both oxide phases. For both materials increasing the temperature, and therefore increasing the oxidation kinetics, leads to a greater reduction in stresses present in both phases and averages. It has been observed that for the ZIRLO™ sample oxidised up to 710 °C (Test A), the stress values become positive after ~73 min. Interestingly the diffraction patterns showed a very weak signal for the beta phase in the metal substrate at this temperature (Fig. 14). This allotropic phase transformation of Zr would result in an expansion in the metal substrate and reduced creep resistance [45], which could drive the oxide stress to become positive.

4.2. Finite element analysis

4.2.1. Stress relaxation

Considering an entirely elastic model of the discussed Zircaloy-4 oxidation in primary water at 360 °C, from an oxide thickness of 0.16 μm-3.3 μm, the average in-plane stress in the oxide is reduced from 1.76 GPa to 1.73 GPa, whilst the average in-plane stress in the metal increases from 0.56 MPa to 11.8 MPa. The volume expansion created by the oxidation of the metal generates a force in both the metal and oxide which is translated into a stress based on the elastic properties and the relative thicknesses of the oxide and the metal. Making the oxide thicker or reducing the thickness of the metal substrate will change the stress balance and increase the tensile stress present in the metal. With the addition of visco-plastic properties the maximum stress in the metal substrate will be limited by creep deformation.

By taking an average of the in-plane stress through the thickness of the model oxide at different time intervals it is possible to compare with the S-XRD data as shown in Figs. 7 and 10–13. Fig. 7 shows that the creep inputs defined for FEA-1 (Section 3.4.1) give a good fit to the stress relaxation defined using S-XRD,

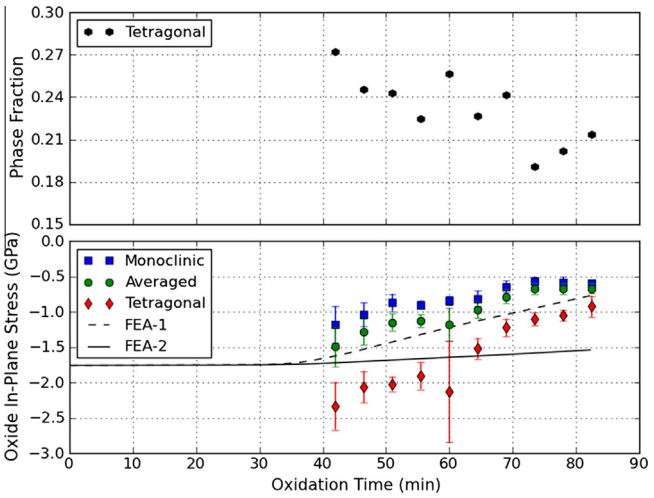

Fig. 10. Zircaloy-4 oxidised up to 710 °C (Test A), showing tetragonal phase fraction (top) and measured monoclinic, tetragonal, averaged, and predicted in-plane oxide bi-axial compressive stresses. FEA-1 uses model parameters fit to the S-XRD data, FEA-2 is based on parameters extrapolated from experimentally defined strain rates.

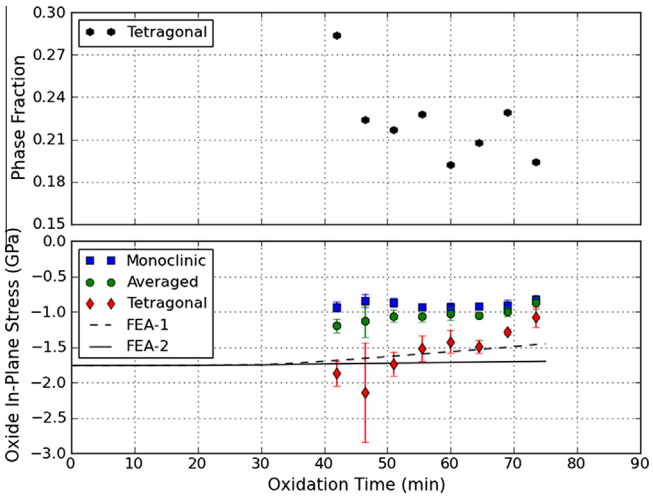

Fig. 11. Zircaloy-4 oxidised up to 650 °C (Test B), showing tetragonal phase fraction (top) and measured monoclinic, tetragonal, averaged, and predicted in-plane oxide bi-axial compressive stresses. FEA-1 uses model parameters fit to the S-XRD data, FEA-2 is based on parameters extrapolated from experimentally defined strain rates.

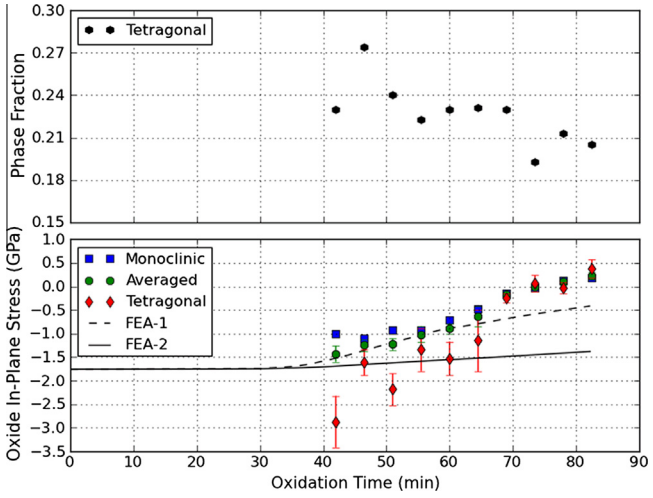

Fig. 12. ZIRLO™ oxidised up to 710 °C (Test A), showing tetragonal phase fraction (top) and measured monoclinic, tetragonal, averaged, and predicted in-plane oxide bi-axial compressive stresses (bottom). FEA-1 uses model parameters fit to the S-XRD data, FEA-2 is based on parameters extrapolated from experimentally defined strain rates.

with the average oxide stress dropping from −1.76 GPa to −1.01 GPa over 220 days and 3.3 μm of oxide growth. However, the resultant strain rate due to creep was $\sim 2.3 \times 10^{-10}\ s^{-1}$. Blat et al. oxidised recrystallised Zircaloy-4 sheet at 360 °C in primary water and recorded strain rates in the order of $\sim 2 \times 10^{-11}\ s^{-1}$ [9]. Barberis et al. oxidised recrystallised M5 sheet in 360 °C water and recorded strain rates in the order of $\sim 5.6 \times 10^{-12}\ s^{-1}$ [10]. Donaldson et al. oxidised tubes of stress relieved cold worked Zircaloy-4 in 350 °C air and recorded axial strain rates of $\sim 4.4 \times 10^{-12}\ s^{-1}$ [13]. These strain rates are an order of magnitude lower than the strain rates shown using the metal creep inputs defined for FEA-1. The fit provided using the inputs for FEA-2 is relatively poor, with the average oxide stress dropping from −1.76 GPa to −1.6 GPa over 220 days and 3.3 μm of oxide growth. However, the resulting creep strain rate is down to $\sim 2.44 \times 10^{-10}\ s^{-1}$, this is typical what should be expected based on the results defined in literature [9,10,13].

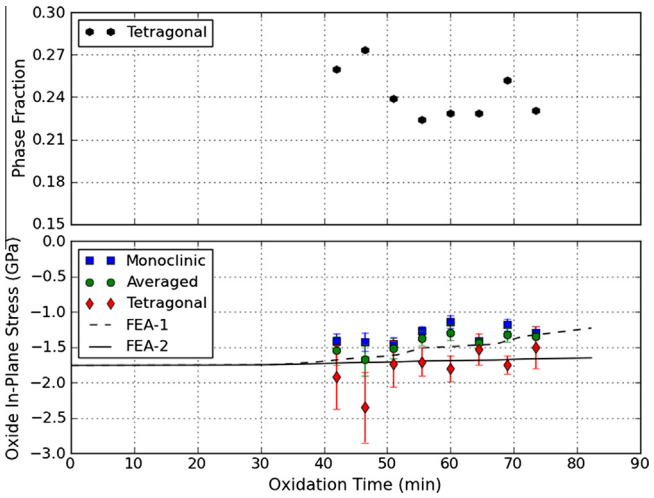

Fig. 13. ZIRLO™ oxidised up to 650 °C (Test B), showing tetragonal phase fraction (top) and measured monoclinic, tetragonal, averaged, and predicted in-plane oxide bi-axial compressive stresses (bottom). FEA-1 uses model parameters fit to the S-XRD data, FEA-2 is based on parameters extrapolated from experimentally defined strain rates.

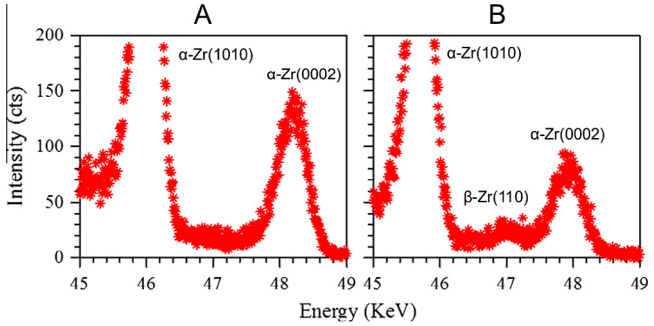

Fig. 14. Diffraction pattern for an oxidised ZIRLO™ sample demonstrating a weak β-Zr peak in the near surface metal substrate (B) which is not present at room temperature (A).

Figs. 10–13 also show the predicted oxide stress for Zircaloy-4 and ZIRLO™ oxidised in air at 710 °C (Test A) and 650 °C (Test B). Air oxidation at high temperatures means that the corrosion kinetics are comparatively fast and the creep strain rates should be accelerated. In spite of the fact the hydrogen-induced lattice strain should not be present during an air oxidation experiment the experimentally observed stress relaxation in the oxide is greater compared to tests carried out at lower temperatures. Although there is some offset in terms of stress, the simulation results given for the model equations defined by FEA-1 give reasonable agreement with the observed trends in stress relaxation. This is the case for both materials and temperature profiles. However, these are based on creep data that gave excessive levels of strain at lower temperatures. As expected, the results based on the model inputs for FEA-2 give much lower levels of stress relaxation. Unfortunately, comparison of oxidation-induced strain rates at these temperatures is not possible, but extrapolation from the lower temperatures indicates that this combination of mechanisms cannot explain the observed stress relaxation.

Significant deviation is seen to occur for the ZIRLO™ material oxidised at 710 °C after ~65 min. The explanation given for this is the formation of β-Zr in the metal substrate detected during the synchrotron experiment (Fig. 14) [46]. This has resulted in the average oxide stress becoming tensile, an effect which cannot

be due to oxidation-induced strain as it is the oxide stress that drives the creep strain in the metal substrate. The stress gradient is steeper for the ZIRLO™ than the Zircaloy-4 meaning more creep has occurred. This is because the thinner metal substrate and thicker oxide layer associated with the ZIRLO™ material creates a greater tensile stress in the metal substrate. It is important to note that the same creep equations and coefficients have been applied to both alloys. The key difference between the materials is the presence of niobium. The maximum solubility of niobium (~0.6 wt%) is lower than the concentration of niobium present in the ZIRLO™ (0.92 wt%) [44]. The remaining niobium forms second phase particles, and as such it is difficult to see how the addition of niobium could impact the diffusion based Coble creep mechanism.

4.2.2. Through oxide stress distributions

The average in-plane stress discussed in the previous section is taken from a series of stress distributions at specific time intervals, defined by the thickness of the partitions shown in Fig. 6 and the specific oxidation kinetics. If the stress relaxation was a result of creep in the metal then it would be expected that there should be a stress gradient through the oxide layer. Fig. 15 shows the distributions in the pre-transition region for the simulation of Zircaloy-4 oxidised in primary water at 360 °C based on the FEA-1 inputs fitted to the observed stress relaxation. In the work by Polatidis et al. efforts were made to assess the through oxide stress distributions based on changes in the diffraction angle [5]. In this case the stress distribution is defined by increasing the depth over which the in-plane oxide stress is averaged. This same averaging approach has been applied to the through oxide stress distribution of Zircaloy-4 oxidised in primary water at 360 °C, based on the FEA-1 inputs at 220 days oxidation, and is compared with SXRD depth distribution data shown in Fig. 16. It can be seen that the fit is poor. This can either be explained as an issue relating to the formation of a network of lateral cracks after ~2 μm oxidation, or simply that the observed stress relaxation is not a product of creep in the metal substrate.

4.2.3. Strain in the metal substrate

For air oxidation the two primary relaxation methods included in the models are creep of the oxide itself and creep of the underlying metal substrate. In the case of autoclave oxidation in primary water, estimates of the hydrogen-induced lattice strain have also been included. Fig. 17 shows total strain, metal creep strain and hydrogen-induced lattice strain for the finite element analysis of Zircaloy-4 oxidised in primary water at 360 °C. This is based on the inputs for FEA-1 for which the metal creep properties were fitted to explain the observed stress relaxation, and FEA-2 for which the properties are defined to so that the oxidation-induced strain is close to that observed in literature. In all of the models analysed creep in the oxide layer was negligible.

Assessing the data in Fig. 17, it can be seen that for FEA-1 the metal creep is very much dominant. However, these strain rates are an order of magnitude greater than anything observed in literature for analysis of oxidation-induced strain [9,10,13]. The results for FEA-2 show that the creep strain rates in the metal substrate are roughly double the hydrogen-induced lattice strain. This is consistent with the final figure shown by Barberis et al. in [10] comparing creep, hydrogen strain and free growth for Zircaloy-4 grid during irradiation at 325 °C in a PWR. This further demonstrates the more appropriate applicability of FEA-2.

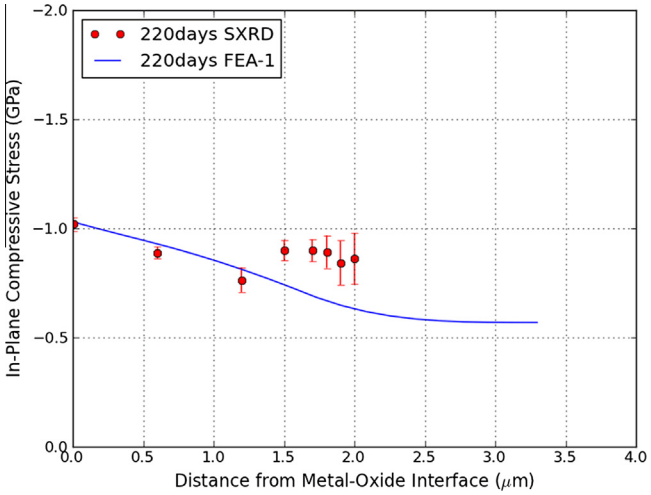

Fig. 16. Shifting average through oxide stress distribution comparing SXRD and FEA based on input FEA-1. FEA-1 uses model parameters fit to the average stress measured using S-XRD.

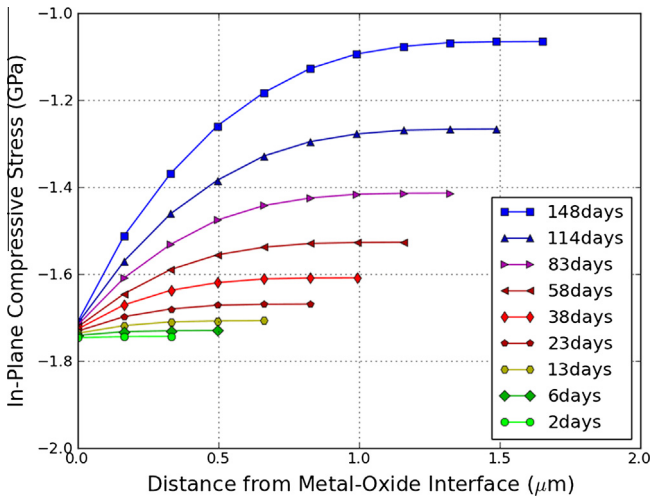

Fig. 15. Stress profiles through the oxide thickness predicted by FEA-1. FEA-1 uses model parameters fit to the average stress measured using S-XRD.

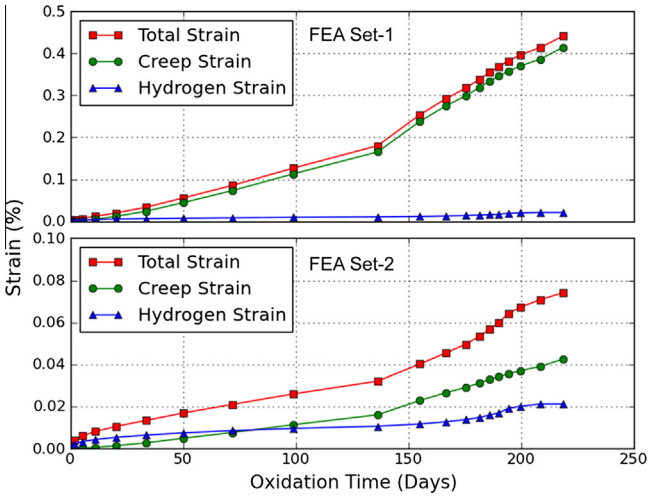

Fig. 17. Metal substrate creep strain predicted by finite element analysis for Zircaloy-4 oxidised at 360 °C in-autoclave. FEA-1 uses model parameters fit to the S-XRD data, FEA-2 gives strain rates similar to those presented by Barberis et al. [10], and Donaldson et al. [13].

4.3. Impact on mechanistic understanding

As discussed, oxides formed on zirconium alloys contain a percentage meta-stable tetragonal phase which is known to be stabilised by the application of an in-plane compressive stress [47]. Hence, relaxation of this stress should reduce the stabilising effect on the tetragonal phase and may partly explain the pre-transition reduction in the tetragonal phase fraction [47,48]. The expansion caused by the phase transformation is known to cause fracture in manufactured stabilised tetragonal zirconia [11], which would allow fast ingress routes into the oxide layer for oxygen containing species.

Comparing with experimental results in literature, finite element analysis has shown that bulk relaxation mechanisms including creep of the oxide layer, creep of the metal substrate, and hydrogen-induced lattice strain are not great enough to explain the observed stress relaxation. As such another mechanism must be responsible for most of the stress relaxation in the oxide observed using S-XRD. Although there is also the possibility of oxygen pick-up during oxidation, this will already be included in the oxidation-induced strains published in literature, which are much lower than that required. More significant may be the development of roughness or undulations at the metal–oxide interface [38,49]. FEA and TEM have both shown that the formation of interface roughness is accompanied by significant localised plastic deformation in the metal substrate [17,50]. Increasing the area of the interface by plastic deformation could potentially reduce the stress in the oxide layer by reducing the constraint. The interfacial roughness has also been associated with strong out-of-plane tensile stress [17], and the formation of small pre-transition lateral cracks and networks of lateral cracks associated with the transition in the corrosion kinetics [5]. EELS analysis has shown that after oxidation the near surface metal contains sub-oxides and regions of oxygen saturated Zr [39]. This oxygen saturation may well impact localised deformation by hardening the substrate and causing localised expansion. However, given the substrate is still constrained by the metal substrate this is expected to have a negligible impact on the macro-scale oxide stress relaxation. Although these features have been observed frequently using both SEM and TEM their impact on the stress state and mechanical behaviour of the oxide has not yet been fully explored and understood [2,3,5,8,51].

5. Conclusions

S-XRD has been used in-situ to analyse the oxides formed on ZIrcaloy-4 and ZIRLO™ during air oxidation at temperatures up to 650 °C and 710 °C. This includes quantifying the stresses in the monoclinic and meta-stable tetragonal phases, and tetragonal phase fraction in the oxide layer. Results indicate a gradual reduction in the residual stress and tetragonal phase fraction. These trends are shown to be similar to samples oxidised in autoclave, with a simulated primary water environment at 360 °C, analysed ex-situ using S-XRD. Results include definition of appropriate thermal profiles and correlating oxidation kinetics.

Based on ex-situ S-XRD data from autoclave oxidised Zircaloy-4, and the current S-XRD analysis of in-situ oxidised Zircaloy-4 and ZIRLO™, finite element analysis has been used to capture some of the mechanical components of the oxidation process. This allows testing of mechanisms that could potentially explain the observed stress relaxation in the oxide layer including; hydrogen-induced lattice strain, oxide creep, and metal creep.

In all of the analyses oxide creep was found to be negligible. When using a set of material inputs that might explain the observed stress relaxation, creep strain rates in the metal substrate are seen to be an order of magnitude greater than any oxidation-induced strain measured in literature. Using creep data and hydrogen-induced lattice strain comparable with literature gave a very low level of stress relaxation. The conclusion from this is that bulk relaxation mechanisms including oxide creep, metal creep and hydrogen-induced lattice strain, are not sufficient to explain the observed stress relaxation. This emphasises the need to understand other mechanical degradation mechanisms, such as the development of roughness at the metal–oxide interface, and lateral cracks in the oxide layer.

Acknowledgements

The authors would like to thank the EPSRC for funding of the Nuclear EngD studentship (Platt), the PhD studentship (Polatidis) and an EPSRC Leadership Fellowship (Preuss). The authors would like acknowledge their collaborators from AMEC, with thanks to Westinghouse for supplying material. Finally grateful acknowledgement is given for the provision of beam time at BESSY II.

References

[1] B. Cox, J. Nucl. Mater. 336 (2005) 331.
[2] A. Yilmazbayhan, E. Breval, A. Motta, R. Comstock, J. Nucl. Mater. 349 (2006) 265.
[3] A. Yilmazbayhan, A. Motta, R.J. Comstock, G.P. Sabol, B. Lai, Z. Cai, J. Nucl. Mater. 324 (2004) 6.
[4] N. Petigny, J. Nucl. Mater. 280 (2000) 318.
[5] E. Polatidis, P. Frankel, J. Wei, M. Klaus, R.J. Comstock, A. Ambard, S. Lyon, R.A. Cottis, M. Preuss, J. Nucl. Mater. 432 (2013) 102.
[6] T. Jacquot, R. Guillén, M. François, B. Bourniquel, J. Senevat, in: Mater. Sci. Forum., Trans Tech Publ, 1996, pp. 845–850.
[7] H.X. Zhang, D. Fruchart, E.K. Hill, L. Ortega, Z.K. Li, J.J. Zhang, J. Sun, L. Zhou, J. Nucl. Mater. 396 (2010) 65.
[8] M. Preuss, P. Frankel, S. Lozano-Perez, D. Hudson, E. Polatidis, N. Ni, J. Wei, C. English, S. Storer, K.B. Chong, M. Fitzpatrick, F. Wang, J. Smith, C. Grosvenor, J. Sykes, A. Cerezo, B. Cottis, S. Lyon, L. Hallstadius, B. Comstock, in: 16th Int. Symp. Zircon. Nucl. Ind., 2010.
[9] M. Blat-Yrieix, a. Ambard, F. Foct, A. Miquet, S. Beguin, N. Cayet, M. Limback, B. Kammenzind, S.W. Dean, J. ASTM Int. 5 (2008) 101321.
[10] P. Barberis, V. Rebeyrolle, J. Vermoyal, in: Zircon. Nucl. Ind. 15th Int. Symp. ASTM STP 1505, 2007, pp. 612–631.
[11] J. Chevalier, L. Gremillard, A.V. Virkar, D.R. Clarke, J. Am. Ceram. Soc. 92 (2009) 1901.
[12] N. Ni, S. Lozano-Perez, M.L. Jenkins, C. English, G.D.W. Smith, J.M. Sykes, C.R.M. Grovenor, Scr. Mater. 62 (2010) 564.
[13] A. Donaldson, Zircon. Nucl. Ind. 9th Int. Symp. ASTM STP 1132 (1991) 177.
[14] D.G. Franklin, R.B. Adamson, J. Nucl. Mater. 159 (1988) 12.
[15] D. Franklin, G. Lucas, A. Bement, Creep of Zirconium Alloys in Nuclear Reactors, ASTM STP 815, 1983.
[16] T.A. Hayes, M.E. Kassner, R.S. Rosen, Metall. Mater. Trans. A 33 (2002) 337.
[17] M. Parise, O. Sicardy, G. Cailletaud, J. Nucl. Mater. 256 (1998) 35.
[18] D.M. Owen, T.G. Langdon, Mater. Sci. Eng., A 216 (1996) 20.
[19] J. Fiala, J. Cadek, Mater. Sci. Eng. 75 (1985) 117.
[20] J. Novotny, J. Fiala, J. Cadek, Acta Metall. 33 (1985) 905.
[21] O. Ruano, J. Wadsworth, O. Sherby, Mater. Sci. Eng. 84 (1986) 1.
[22] J. Wadsworth, O. Ruano, O. Sherby, Metall. Mater. Trans. A 33A (2002).
[23] F. Gutierrezmora, J. Eur. Ceram. Soc. 22 (2002) 2615.
[24] D. Owen, A. Chokshi, Acta Mater. 46 (1998) 667.
[25] M.J. Roddy, W.R. Cannon, G. Skandan, H. Hahn, J. Eur. Ceram. Soc. 22 (2002) 2657.
[26] A. Chokshi, Scr. Mater. 48 (2003) 791.
[27] A. Chokshi, J. Eur. Ceram. Soc. 22 (2002) 2469.
[28] S. Ghosh, S. Swaroop, P. Fielitz, G. Borchardt, A.H. Chokshi, J. Eur. Ceram. Soc. 31 (2011) 1027.
[29] M. Matsuda, Solid State Ionics 111 (1998) 301.
[30] K. Kowalski, A. Bernasik, A. Sadowski, J. Eur. Ceram. Soc. 20 (2000) 2095.
[31] K. Kowalski, A. Bernasik, A. Sadowski, J. Eur. Ceram. Soc. 20 (2000) 951.
[32] S. Swaroop, M. Kilo, C. Argirusis, G. Borchardt, A. Chokshi, Acta Mater. 53 (2005) 4975.
[33] P. Vizcaíno, Engineering 02 (2010) 573.
[34] J. Wei, P. Frankel, M. Blat, A. Ambard, R.J. Comstock, L. Hallstadius, S. Lyon, R.A. Cottis, M. Preuss, Corros. Eng., Sci. Technol. 47 (2012) 516.
[35] C. Genzel, I.A. Denks, J. Gibmeier, M. Klaus, G. Wagener, Detect. Assoc. Equip. 578 (2007) 23.
[36] R. Garvie, P. Nicholson, J. Am. Ceram. Soc. (1972) 303.
[37] K. Park, Y. Chun, J. Korean Nucl. Soc. (1997).
[38] P. Bossis, F. Lefebvre, P. Barbéris, A. Galerie, Mater. Sci. Forum 369–372 (2001) 255.
[39] N. Ni, S. Lozano-Perez, J. Sykes, C. Grovenor, Ultramicroscopy 111 (2011) 123.

[40] P. Platt, P. Frankel, M. Gass, R. Howells, M. Preuss, J. Nucl. Mater. 454 (2014) 290.
[41] B. Cox, V. Kritsky, C. Lemaignan, V. Polley, I. Richtie, H. Ruhmann, V. Sishov, IAEA TECDOC 996 (1998).
[42] K. Videm, Nucl. Eng. Des. 21 (1972) 200.
[43] S. MacEwen, C. Coleman, C. Ells, Acta Metall. 33 (1985) 753.
[44] I. Charit, K. Murty, J. Nucl. Mater. 374 (2008) 354.
[45] M.R. Daymond, R.a. Holt, S. Cai, P. Mosbrucker, S.C. Vogel, Acta Mater. 58 (2010) 4053.
[46] E. Polatidis, Residual Stress and Phase Characterisation on Zirconium Oxides Using Synchrotron X-ray Diffraction, The University of Manchester, 2012.
[47] R.C. Garvie, J. Phys. Chem. 82 (1978) 218.
[48] W. Qin, C. Nam, H.L. Li, J.A. Szpunar, J. Alloys Compd. 437 (2007) 280.
[49] P. Tejland, H.-O. Andrén, J. Nucl. Mater. 430 (2012) 64.
[50] P. Tejland, H.-O. Andrén, J. Nucl. Mater. 444 (2014) 30.
[51] D. Hudson, N. Ni, S. Lozano-Perez, D. Saxey, C. English, G.D.W. Smith, J. Sykes, C. Grovenor, Users.ox.ac.uk (n.d.).
[52] N. Prasad, G. Malakondaiah, P.R. Rao, Scr. Metall. 26 (1992) 541.